

Influence of ENSO on the Pacific Decadal Oscillation in CMIP models

**AG Nidheesh¹, Matthieu Lengaigne^{2,3}, Jérôme Vialard², Takeshi Izumo^{2,3}, AS
Unnikrishnan¹, Christophe Cassou⁴**

¹ CSIR-National Institute of Oceanography (NIO), Goa, India

² Sorbonne Universités (UPMC, Univ Paris 06)-CNRS-IRD-MNHN, LOCEAN Laboratory, IPSL,
Paris, France

³ Indo-French Cell for Water Sciences, IISc-NIO-IITM-IRD Joint International Laboratory, NIO,
Goa, India

⁴ CNRS-Cerfacs, Global Change and Climate Modelling project, 42 Avenue G Coriolis, 31057
Toulouse, France.

To be submitted to Climate Dynamics

Corresponding author:

A.G. Nidheesh

Physical Oceanography Division
CSIR-National Institute Of Oceanography
Dona Paula - Goa - 403004 India
Email: nidheeshag@gmail.com

Abstract

Emerging decadal climate predictions call for an assessment of decadal climate variability in the Coupled Model Intercomparison Project (CMIP) database. In this paper, we evaluate the influence of El Niño Southern Oscillation (ENSO) on Pacific Decadal Oscillation (PDO) in 10 control simulations from the CMIP3 and 22 from the CMIP5 database. All models overestimate the time lag between ENSO forcing and the PDO response. While half of the models exhibit ENSO-PDO correlation which is close to that in observation (> 0.5) when the time lag is accounted for, the rest of the models underestimate this relationship. Models with stronger ENSO-PDO correlation tend to exhibit larger PDO-related signals in the equatorial and south Pacific, highlighting the key role of ENSO teleconnection in setting the inter-hemispheric Pacific pattern of the PDO. The strength of the ENSO-PDO relationship is related to both ENSO amplitude and strength of ENSO teleconnection to the North Pacific sea-level pressure variability in the Aleutian Low region. The shape of the PDO spectrum is consistent with that predicted from a combination of direct ENSO forcing, atmospheric stochastic forcing over the North Pacific and the re-emergence process in 27 models out of 32. Given the essential role of ENSO in shaping the Pacific decadal variability, models displaying realistic ENSO amplitude and teleconnections should be preferentially used to perform decadal prediction experiments.

Key words: ENSO, PDO, Decadal variability, Climate, CMIP

1. Introduction

The El Niño-Southern Oscillation (ENSO) is the leading mode of global interannual climate variability (e.g. McPhaden et al. 2006). El Niño manifests itself in the central and eastern tropical Pacific Ocean as a widespread Sea Surface Temperature (SST) warming (Fig. 1a), that enhances deep atmospheric convection and tropospheric diabatic heating over the central Pacific. This diabatic heating drives an atmospheric planetary wave response, resulting in global-scale impacts through atmospheric teleconnections (e.g. Alexander et al. 2002). This response is indeed channelled toward higher latitudes by the zonal mean circulation, acting to deepen the extra-tropical low pressure systems and strengthen the westerlies over the North and South Pacific (see Fig. 1a and e.g. Alexander 1990; Lau and Nath 1994; Lau and Nath 1996; Alexander et al. 2002). ENSO also affects the rest of the tropics via zonal shift of the Pacific Walker circulation (e.g. Klein et al. 1999; Lau and Nath 2000). The atmosphere thus acts like a bridge linking the tropical Pacific variability to sea level pressure and surface wind variations in other oceanic regions, leading to clear heat flux and SST signature of El Niño outside the tropical Pacific (e.g. Zhang et al. 1997), resulting in positive SST anomalies in the central equatorial Pacific surrounded by anomalies of opposite polarity in the western tropical Pacific extending poleward into the central North and South Pacific (i.e. the well known “horseshoe” pan-Pacific SST pattern of El Niño) as seen in Fig. 1a.

ENSO exhibits its most energetic fluctuations at interannual time scales but also displays lower-frequency fluctuations at decadal/multi-decadal time scales (Fig 1bc). Recent studies have illustrated a “pacemaker” role of ENSO on global SST at both interannual and decadal time scales. The global surface warming slowdown during the last decade (Easterling and Wehner 2009), often referred to as a “hiatus” in global warming, has indeed been attributed to natural climate variability associated with decadal ENSO variations (e.g. Meehl et al. 2011; Kosaka and Xie 2013; England et al. 2014), arising through an increased heat uptake of the tropical Pacific Ocean, associated with the more frequent occurrence of La Niña events over the last fifteen years. The influence of ENSO on the low-frequency evolution of global temperature clearly illustrates the need to better understand the global impacts of ENSO, especially at decadal time scales.

The most prominent structure of decadal SST variability in the North Pacific is named the Pacific Decadal Oscillation (PDO; e.g. Zhang et al. 1997; Mantua et al. 1997). This SST pattern largely results from fluctuations of the North Pacific Aleutian Low (Pierce et al. 2000; Alexander et al. 2002), either intrinsic or modulated by ENSO forcing through the aforementioned atmospheric bridge (Alexander 1990; Lau and Nath 1994; Lau and Nath 1996; Alexander et al. 2002). The influence of ENSO translates into a ~ 0.6 correlation between ENSO and PDO time series (Fig. 1b

and 1e) in observation, with ENSO leading the PDO evolution by 1-2 months. As a result, the pan-Pacific expression of the PDO, known as the Inter-decadal Pacific Oscillation (Power et al. 1999; Folland 2002), bears a strong resemblance with that of ENSO, except for a stronger weighting in the North Pacific relative to the tropical Pacific (Fig. 1a and 1d). The North Pacific SST anomalies resulting from the combined influence of ENSO and stochastic forcing in the North Pacific are detrained from the mixed layer at the end of each winter and persist in the seasonal thermocline through summer, isolated from the atmospheric influence. Part of those anomalies « re-emerge » through entrainment into the mixed layer during the following winter (Namias and Born 1974; Alexander and Deser 1995; Deser et al. 2003). Thus the long-term integration of the atmospheric forcing by the ocean (e.g. Frankignoul and Hasselman 1977; Vimont 2005) results in an increase of the PDO variance in the low frequency part of its spectrum, i.e. at decadal and multi-decadal time scales (Fig. 1ef). Newman et al. (2003) showed that the observed PDO spectrum was compatible with that obtained from a simple auto-regressive model accounting for ENSO influence, stochastic atmospheric forcing and re-emergence process. In this paradigm, the PDO can be described as a reddened response to both ENSO and atmospheric stochastic forcing over the North Pacific. There are however evidences that the North Pacific gyre anomalies and local air-sea coupling processes also contribute to the Pacific climate variability at multi-decadal time scales (e.g. Deser and Blackmon 1995; Wu et al. 2003; Schneider and Cornuelle 2005; Qiu et al. 2007; Di Lorenzo et al. 2008), leading other authors to suggest that the PDO may not be explained from a single physical mode but rather the sum of several phenomena (Schneider and Cornuelle 2005; Liu 2012; Newman 2013; Newman et al. 2016).

Projections of the climate system response to anthropogenic forcing are generally derived from the analysis of simulations from the Coupled Model Intercomparison Project (CMIP) database (Meehl et al. 2007; Taylor et al. 2012). The aforementioned importance of Pacific decadal variability for hiatus periods in observations stresses the need to evaluate how these models capture the internal decadal climate variability (Meehl et al. 2014). Some of the previous studies concluded that, most of the models from the CMIP3 database reproduce the spatial pattern of the PDO in the North Pacific reasonably well, despite a large diversity in its amplitude (Furtado et al. 2011; Kwon et al. 2012; Park et al. 2013; Yim et al. 2014). However it has also been reported that the influence of ENSO on the PDO is considerably underestimated or even non-existent in most CMIP simulations (Newman 2007; Oshima and Tanimoto 2009; Furtado et al. 2011; Deser et al. 2012; Park et al. 2013). For instance, Furtado et al. (2011) concluded that only one third of the CMIP3 models display significant (but underestimated) correlation between ENSO and the PDO. While Furtado et al. (2011) suggested

that this mismatch arises from a weak projection of ENSO atmospheric teleconnection onto the Aleutian Low (AL) due to a misrepresentation of its geographic location in most of the models, Park et al. (2013) pointed towards the model's deficiency in simulating ENSO amplitude and centres of actions. In contrast, Lienert et al. (2011) showed that the simulated amplitude of ENSO-related signals in the North Pacific as well as the time-lag between PDO and ENSO were overestimated in these models possibly because of an overestimated mixed layer depth and underestimated air-sea feedbacks in the North Pacific.

In the present paper, we will extend the analyses of Newman (2007), Oshima and Tanimoto (2009), Furtado et al. (2011), Deser et al. (2012) and Park et al. (2013) to the CMIP5 database, which is used in the fifth Intergovernmental Panel on Climate Change (IPCC) assessment report. Section 2 describes the selected models (10 from CMIP3 and 22 from CMIP5), the observational (reference) datasets, and the analysis methods. Section 3 discusses the large diversity in the ENSO-PDO relationship in CMIP models and its consequences on the Pan-Pacific PDO patterns. The reasons behind the diversity in the ENSO-PDO relationship in CMIP models are addressed in Section 4. Section 5 provides a summary of our results and a discussion in the context of other relevant studies.

2. Data and methods

2.1. Observational data

As our goal is to describe interannual to decadal SST variations in the Pacific Ocean, we considered only those observational datasets, which span at least the entire 20th century. To infer the robustness of our conclusions regarding PDO characteristics in observations, we analysed three gridded SST products. Our baseline dataset is the HadISST dataset available from 1870 onwards. It is based on blended in-situ and satellite data sources after 1981 and sparse ship datasets before (Rayner et al. 2003), with an optimal interpolation to fill the gaps in data-sparse oceanic regions. We compared the results obtained from HadISST with two other SST reconstruction products that also use blended in-situ and satellite data and statistical techniques to fill the gaps: ERSSTv3 available from 1854 (Smith et al. 2008) and Kaplan-v2 available from 1856 (Kaplan et al. 1998). We also used surface wind stress, mean sea-level pressure (SLP) and precipitation fields from the twentieth century (20thC) reanalysis (Compo et al. 2011). This atmospheric reanalysis, available from 1870 to 2012, assimilates surface and SLP observations from the International Surface Pressure Databank station component version 2 (Yin et al. 2008), from the International Comprehensive Ocean–Atmosphere Data Set (ICOADS, Woodruff et al. 2011) and from the International Best Track Archive for Climatic Stewardship (IBTrACS; Knapp et al. 2010). To allow for a fair comparison, all

these datasets are interpolated onto a common $2.5^{\circ} \times 2.5^{\circ}$ horizontal grid (i.e. the regular NCEP grid) and are analysed at monthly resolution over their common period, i.e. 1871-2010.

2.2. CMIP models

We analysed models from both CMIP3 (Meehl et al. 2007) and CMIP5 (Taylor et al. 2012) archives in this study. To avoid potential aliasing of the natural variability by anthropogenic forcing, we focused on multi-century pre-industrial control simulations, with a constant CO_2 concentration of about 280 ppm. As the focus of the present study is on decadal variability (~ 8 to 30 years periods), we analysed only those models that provide at least 250 years of simulations to ensure statistical robustness of the spectral characteristics of modelled decadal variability. This criterion has led to the selection of 10 CMIP3 and 22 CMIP5 simulations which are listed in Table 1. Our analyses are based on outputs of monthly-mean SST, wind, SLP and precipitation fields, interpolated onto a common $2.5^{\circ} \times 2.5^{\circ}$ horizontal grid.

2.3. Climate indices definition

Following Zhang et al. (1997) and Mantua et al. (1997) seminal papers, PDO-related literature usually defines the PDO from the leading EOF of monthly SST anomalies over the North Pacific after removing the global mean SST time series. We used a similar method in the present study. SST anomalies are calculated by removing the monthly climatology. The global mean SST and a linear trend are then removed from each grid point and a five-month running mean is applied before performing the EOF analysis. Note that the results in this study are insensitive to avoiding this 5-month smoothing and that a similar kind of time series smoothing has been applied in other studies (e.g. a 3-month smoothing in Newman et al. 2003). For the PDO, the EOF is performed over the 110°E - 110°W ; 20°N - 60°N region. Similarly, ENSO variability is defined as the leading EOF of the monthly SST anomalies over the tropical Pacific (120°E - 80°W ; 20°N - 20°S) as defined in (Newman et al. 2003). The first EOF over the North (tropical) Pacific and corresponding principal component are used to define the PDO (ENSO) pattern and time evolution. The EOF spatial pattern is normalized (i.e. divided) by its spatial root mean square (RMS) over either the tropical (ENSO) or North Pacific (PDO) where EOF is performed. The corresponding PC is then multiplied by this RMS value so that the PC accounts for the amplitude of either ENSO or the PDO. The standardised global/regional signature associated with these climate mode is computed by regressing different variables (SST, SLP, wind and precipitation) onto the corresponding PC time series. As stated in the introduction, variability in the Aleutian Low central pressure, either internally driven or remotely-forced by ENSO, plays a central role in forcing the PDO in the North Pacific. In this paper, we

identify the Aleutian Low variability as the first EOF of SLP over the North Pacific (110°E-110°W; 20°N-60°N - region similar to that used to define the PDO) and the associated PC is used as an index of this Aleutian Low.

The interannual and decadal components of the ENSO-PDO time series and all the variables discussed in this study are extracted using the STL (Seasonal-Trend decomposition) filtering method (Cleveland et al. 1990). STL is a robust iterative non-parametric regression procedure using a Loess smoother, which allows decomposing a time series into seasonal, interannual and decadal (long-term) components. As for all non-parametric regression methods, STL requires subjective selection of a smoothing parameter to define the lowest frequency component. We have chosen a 7-year threshold to extract decadal component of the various datasets.

2.4. Spectral analysis

As stated in the introduction, re-emergence of North Pacific SST anomalies from the previous winter, ENSO forcing through mid-latitude teleconnections and the atmospheric white noise forcing are the key components in setting the temporal characteristics of the PDO variability. Newman et al. (2003) built a simple linear model of the PDO evolution that incorporates these three processes (equation 1). We use a similar definition of ENSO and PDO indices to Newman et al. (2003) when deriving this model. In Newman et al. (2003), PDO and ENSO indices for *year n* are computed as annual values obtained from the July (n) to June (n+1) average, in order to account for the fact that ENSO and the PDO are both maximum in boreal winter. Hence the PDO evolution is modelled using a first-order auto-regressive (AR-1) model as:

$$P_n = \alpha P_{n-1} + \beta E_n + \eta_n \quad (1)$$

where P is the normalized (divided by the standard deviation of the time series) PDO index, E is the normalized ENSO index, n is time (in years), and η is the (unpredictable) atmospheric white noise. The β parameter is obtained by regressing the PDO index onto the ENSO index. The α parameter is obtained by regressing the residual ($P_n - \beta E_n$) on the previous year's PDO index P_{n-1} . Hence for this model, α represents the strength of the re-emergence process while β accounts for the influence of ENSO on the PDO.

Applying this AR-1 model to HadISST data over the 1900-1999 period, Newman et al. (2003) showed that the model PDO time series yields a 0.74 correlation with observed PDO index, a significantly better skill than when only either ENSO or re-emergence is accounted for. They also concluded that the observed spectrum is well within the 95% confidence interval of the spectrum derived from the AR-1 model, suggesting that the observed PDO evolution can largely be explained

by accounting only for atmospheric stochastic forcing, re-emergence and ENSO forcing. The relatively short (100 years) observational record however translates into strong uncertainties in the spectrum at decadal and multi-decadal time scales. As suggested by Schneider and Cornuelle (2005), this simple analysis does not preclude other processes, such as changes in the gyre circulation in the North Pacific, to operate. To assess the role of ENSO onto the PDO in CMIP simulations, we applied the simple model described by equation (1) to the CMIP PDO time series as described in Section 3.1.

To calculate the PDO power spectrum, the PDO index defined in section 2.3 as the leading PC in the North Pacific, is first converted into June-July averaged yearly values and then normalized by its standard deviation to have unit variance. A Fourier transform is then applied to obtain the raw power spectrum. To reduce the statistical noise which is inherent to spectrum calculation of finite time series, we use the Daniel's estimator approach (well-suited for the case of continuous time series as in the present study), with the Daniel's filter being here a triangle filter to reduce noise: a N -point double running-mean (i.e. a triangle filter of $2N$ length) is used, where N has to be chosen to give a good compromise between accurate amplitude and accurate bandwidth (see von Storch and Zwiers 1999 for details). We have found $N=3$ to be adequate for the 140 years-long observational record over the 1871-2010 period. For CMIP models, we chose N as the integer closest to $3N_y/140$ (where N_y is the number of years of simulation available for a given CMIP model) to obtain a comparable bandwidth to that obtained for observations which allows a fair comparison. This choice results in a similar spectral resolution for all computed spectra.

The PDO power spectrum is then compared to the spectrum computed from Newman's model (eq. 1). For this purpose we used a similar approach as Newman et al. (2003). Three steps are necessary. First, we generate 1000 white noise time series (random time series), with the amplitude of the noise defined by the standard deviation of the residual in equation (1) (i.e. the time series obtained once the ENSO and re-emergence influence is removed linearly from the original PDO time series). This allows generating 1000 samples of synthetic PDO time series (referred as "*model time series*" in the text) and thus to calculate 1000 *model* power spectra. The mean of these 1000 spectra is considered as the average Newman's model spectrum and the 2.5th and 97.5th percentiles of the spectral estimate distribution are used to establish the 95% confidence interval around the average model PDO spectrum.

3. ENSO-PDO relationship in CMIP models

Observations indicate that PDO is partly driven by the tropical Pacific variability associated with ENSO (Garreaud and Battisti 1999; Newman et al. 2003; Shakun and Shaman 2009). In this section,

we will first show that the PDO tends to lag much more ENSO in CMIP models than in observations and that the influence of ENSO on the PDO is underestimated in models if this lag is not taken into account. However, the strength of the ENSO-PDO relationship varies considerably amongst CMIP models and holds a key-role in shaping the PDO pan-Pacific spatial pattern.

Figure 2 displays the maximum lag-correlation between ENSO and PDO indices (and corresponding lag) for all observational and CMIP datasets at interannual and decadal time scales combined (Fig. 2a; referred as "All time scales" hereafter) and separately for interannual and decadal time scales (Fig. 2bc). For a fair comparison with estimates from observation, the transparent frames shown at the tip of each bar indicate the minimum and maximum lag-correlation obtained by sub-sampling each model time series over 140-years sliding windows (i.e. the length of the observational record). In observations, the correlation between ENSO and PDO time series ranges from 0.52 for ERSST dataset to 0.61 for Kaplan, with ENSO leading the PDO by one to two months (Fig. 2a; black bars). As in observations, ENSO systematically leads the PDO in all CMIP models. Except for the FIO model, this lead-time is however larger in CMIP models (from 3 to 8 months) than in observations (~1-2 months). Previous studies that examined the links between ENSO and the PDO did not account for this lag but estimated the ENSO-PDO relationship based on instantaneous correlations (e.g. Furtado et al. 2011, Park et al. 2013). Figure 3 compares the maximum lag- and instantaneous-correlation between ENSO and the PDO. In observations, the instantaneous and lag correlations are quite close due to the small lag (~1 month) between ENSO and the PDO. In CMIP models, however the instantaneous correlation is consistently (0.1 to 0.3) smaller than the lag correlation, due to the overestimated lag in CMIP models. Analysis based on instantaneous correlations (Furtado et al. (2011) and Park et al. (2013)) concluded that the influence of ENSO on the PDO is underestimated in CMIP models. Figure 3 however shows that accounting for the lag between ENSO and the PDO in models allows to define a group of models for which the ENSO-PDO links are in qualitatively agreement with observations.

When accounting for this lag, CMIP models exhibit a large range of ENSO-PDO correlations (Fig. 2a) with all correlations being significant and varying from 0.15 to 0.75. 17 models exhibit a maximum ENSO-PDO lag-correlation within the range of that observed (> 0.5 ; shown by green bars) while the remaining 15 models underestimate the ENSO-PDO relationship (red bars). In the following, we further divide CMIP models into two classes depending on the strength of the simulated ENSO-PDO relationship. We define Class-I models as those with a maximum ENSO-PDO lag-correlation above 0.5 (green bars in Fig. 2a). These models exhibit an average correlation of 0.58 very close to the observational average (thick black bar on Fig. 2a). The black frames provide an

indication of the possible range on ENSO/PDO correlation when calculating these correlation over the same length as the observational records (140 years). The typical correlation spread reaches 0.15, but considerably varies from one model to another. A large fraction of the variation of this correlation for a given model is likely to arise from the internal variability of each model, as illustrated by Deser et al. (2014, 2016) for the case of the air temperature over north America. It must however be noticed that a proper estimation of the internal variability in each model would require either longer pre-industrial simulations or large single model ensembles (Deser et al. 2012). Considering this uncertainty, all individual model within Class-I models except one exhibit correlations within the range of observed estimates (between 0.52 and 0.61; see black frames on Fig. 2a). Class-II models are defined as models with a maximum ENSO-PDO lag-correlation below 0.5 (with an average correlation of 0.35 that is weak compared to that deduced from observations; red bars in Fig. 2a). Most of the Class-II individual models indeed exhibit correlations systematically below the range of the observed estimates within the uncertainty limits (see black frames on Fig. 2a). It has to be noticed that a larger proportion of CMIP3 models falls into Class-II models (7 models) compared to Class-I models (3 models).

Re-computing these statistics separately for interannual and decadal components of ENSO and PDO time series (Fig. 2bc) illustrates that the observed ENSO-PDO relationship is slightly stronger at decadal (correlation of ~ 0.7) than at interannual time scales (~ 0.55). This is expected as applying decadal smoothing acts to decrease the noise of the time series. However, the difference in correlation found in observation between these two time scales is not so apparent in CMIP models. In addition, models with large ENSO-PDO lag-correlation at interannual time scales also generally display large lag-correlation at decadal periods with Class-I and Class-II models respectively displaying an average maximum lag-correlation of 0.6 / 0.38 at interannual and 0.58 / 0.36 at decadal time scales. As expected, CMIP correlation uncertainties are generally larger at decadal than at interannual time scales (see black frames on Fig. 2bc): this results in ENSO-PDO lag-correlations falling within the observed range at decadal time scales for two third of CMIP models. This analysis also reveals that ENSO systematically leads the PDO at both time scales, with a tendency for the lag to be larger at decadal time scales (~ 8 months vs ~ 4 at interannual time scales). This systematic tendency of ENSO to lead the PDO across models and observation suggests that ENSO forces the PDO, rather than the other way around.

To quantify more precisely how much of the PDO can be explained as a reddened response to ENSO and atmospheric stochastic forcing, we fit an AR-1 model proposed by Newman et al. (2003; eq. (1) in Section 2.4) to the PDO time series from the three observational and 32 CMIP simulations.

Figure 4a evaluates the performance of this AR-1 model in capturing the PDO variability. The influence of ENSO forcing on the PDO evolution is represented by the β coefficient in equation (1), shown on Figure 4b. In line with Newman et al. (2003) results, this AR-1 model accurately captures the PDO variability in observations, with a skill (which is defined as the correlation between the original PDO time series and the PDO time series predicted by eq. 1) ranging between 0.67 and 0.73 depending on the observational dataset considered (black bars on Fig. 4a). This AR-1 model also performs generally better in reproducing Class-I models PDO evolution: all Class-I models except one exhibit a correlation above 0.6, with a 0.67 average correlation that is very close to observation. In contrast, the average skill of Class-II models is 0.4 and all Class-II models tend to exhibit a weaker correlation than Class-I models. As expected from the ENSO-PDO correlations shown on Figure 2a, there is a striking difference on the β values of Class-I and Class-II models, with a larger ENSO influence on PDO for Class-I models. However, the influence of ENSO as depicted by the β coefficient is generally weaker in CMIP models than in observational products, which may be related to the overestimated response time of the PDO relative to ENSO forcing in CMIP models, which we did not account for when deriving the AR-1 model.

The AR-1 model (eq. 1) also allows testing whether the reddened response to ENSO and atmospheric white noise can explain the PDO spectral characteristics in CMIP models. As an illustration, Figure 5 compares the actual PDO spectrum with that derived from the AR-1 model for HadISST and two selected models with contrasted behaviours. Accounting for the influence of ENSO on the PDO allows reproducing most of the PDO spectral peaks at interannual time scale and the red-noise behaviour at decadal time scales in HadISST data (Fig. 5a). In line with Newman et al. (2003) results, the observed PDO spectrum is therefore well captured by the reddened response to ENSO and atmospheric white-noise forcing (this is also the case in other observed datasets but not shown). As for observations, the PDO spectrum of the MIROC5 model (which displays the highest skill and ENSO influence on PDO, see Fig. 4) is very close to that derived from equation (1) (Fig. 5b) and lies within the 95% confidence interval of the mean model spectrum. In fact, the actual PDO spectrum lies well within the confidence interval of the AR-1 model spectrum for 27 out of the 32 CMIP models analysed in this study. This suggests that the PDO spectral characteristics can be understood as a reddened response to ENSO and atmospheric white noise forcing in most CMIP models. Only 5 models out of 32 (four of them belong to Class-II), exhibit a spectral peak at decadal time scales that cannot be explained by the AR-1 model (see Table 2). This is for instance the case for BCC-CSM1 (Fig. 5c), which displays a peak around 12 year period that lies outside the confidence level. There are thus only 5 models out of 32, for which PDO spectral characteristics

cannot be explained from the three basic processes encapsulated in Newman et al. (2003) model: ENSO forcing, stochastic forcing and oceanic memory due to re-emergence processes, i.e. for these 5 models, other processes (such as changes in oceanic gyre circulation associated with the Kuroshio extension) need to be accounted for to explain the PDO spectral characteristics at decadal time scales.

Figure 6 illustrates how the diversity of the simulated ENSO-PDO relationship across the CMIP models translates into their ENSO and PDO pan-Pacific patterns. The observed pan-Pacific signature of ENSO is displayed on Figure 6a. As expected, the observed ENSO pattern is characterized by an equatorial Pacific warming associated with tropical SLP seesaw and converging westerly wind anomalies west of the maximum warming (Fig. 6a). The ENSO pattern also exhibits a strong extra-tropical signatures over both hemispheres. For instance, a broad area of negative SLP anomalies characterize the central and eastern North Pacific, near the Aleutian Low climatological position. In this region, anomalous surface winds are roughly in geostrophic balance with the Aleutian Low fluctuations, with maximum westerly and negative SST anomalies south of the anomalous low (highlighted by the grey dashed frame on Fig. 6a). By similar mechanisms as in the North Pacific (Shakun and Shaman 2009), a sea-surface cooling is also observed in the South Pacific and is associated with westerly wind anomalies equator-ward of the maximum negative SLP anomalies (Fig. 6a). The ENSO pan-Pacific signature on Figure 6a is very robust between different observed datasets, with SST pattern correlation exceeding 0.95 (black bars, Fig. 6g). Both Class-I and Class-II models accurately reproduce the observed pan-Pacific ENSO pattern (Fig. 6a-c), with only three models having pattern correlation below 0.75 (Fig. 6g). Both classes of models are able to accurately simulate the location and amplitude of the negative SLP signature over the North Pacific and the associated westerly anomalies south of it (Fig. 6bc). Class-I and Class-II models however share some common biases, such as a westward shift of the equatorial warming and of the North Pacific cooling. The only apparent difference between the two classes of models relates to the amplitude of the low pressure and cooling signals in North Pacific, which are generally slightly weaker in Class-II compared to Class-I models (Fig. 6bc).

A similar analysis is provided for the pan-Pacific signature of the PDO on Figure 6d-f and 6h. In observations, the pan-Pacific expression of the PDO bears a strong resemblance with that of ENSO (Fig. 6a and 6d), except that for the PDO there is a stronger weighting in the North Pacific relative to the tropical Pacific. In particular, the PDO is related to a negative SLP pattern within the Aleutian Low region (Fig. 6d), very similar to the ENSO SLP signature in that region (Fig. 6a). As for ENSO, the observed pan-Pacific PDO pattern is very robust between different observational

datasets, with SST pattern correlation exceeding 0.95 (black bars, Fig. 6h). Both Class-I and Class-II models capture the PDO SST signature and the location and spatial extent of the related SLP and wind signal reasonably well over the North Pacific (Fig. 6ef). One obvious caveat of all CMIP models is however a clear westward shift of the maximum SST anomalies in the North Pacific, which are located in the Kuroshio extension region in models, rather than $\sim 160^\circ\text{W}$ as seen in observations. This may be related to the tendency of model SLP and wind perturbation to extend further westward (Fig. 6d-f) or to systematic errors in the mixed layer depth distribution (Lienert et al. 2011).

While Class-I and II CMIP models behave in a rather consistent way over the North Pacific, they exhibit a large diversity in reproducing the pan-Pacific signature of the PDO, with SST pattern correlations with HadISST ranging from 0.4 to 0.82. There is also a clear tendency for Class-I pattern to agree more with observations than Class-II models (Fig. 6h), with average pattern correlation of 0.8 and 0.65 respectively. As shown on Figure 7a, there is indeed a strong relationship (0.7 correlation) between the ENSO-PDO maximum lag-correlation (i.e. the criteria used to classify the CMIP models) and the quality of the simulated pan-Pacific PDO pattern: models that reproduce the observed pan-Pacific PDO pattern well are those who display a strong influence of ENSO on the PDO. Figure 6ef indicate that a large part of the pan-Pacific PDO pattern difference between Class-I and Class-II models arises from the signal outside the North Pacific region: Class-I models have a larger equatorial and South Pacific SST and SLP signature compared to Class-II models, although still weaker than in observations (Fig. 6d-f). This relationship is further quantified in Figure 7b. There is a 0.84 correlation between the quality of the model pan-Pacific PDO pattern and the equatorial warming associated with the PDO. Similarly, the amplitude of the sub-tropical southern Pacific signal is also clearly related to the amplitude of the equatorial warming (0.88 correlation; Fig. 7c), with an underestimated South Pacific cooling signal in Class-I models but almost non-existent in Class-II models. Most of the differences in the Class-I and Class-II models pan-Pacific PDO pattern thus arise from the differences in the relative amplitude of the SST signal associated with the PDO over the tropical and South Pacific regions. Models that reproduce the pan-Pacific PDO pattern reasonably well are those with a larger equatorial and south Pacific SST signal for a given amplitude of the North Pacific signal. In the following section, we investigate possible reasons that can explain the diversity of the ENSO-PDO relationship in CMIP models.

4. Explaining the diversity of ENSO influence on the PDO in CMIP models

As mentioned in the introduction, El Niño influences North Pacific SST through the atmospheric bridge: warm SST anomalies in the equatorial Pacific enhance rainfall and the

associated diabatic heating, inducing upper-level tropospheric divergence over the central tropical Pacific. This heating forces Rossby waves that are channelled by the mean circulation toward the North Pacific (e.g. Trenberth et al. 1998), strengthening the Aleutian Low (e.g. Alexander et al. 2002; see Fig. 6a). The resulting westerly anomalies to the south of the Aleutian Low combine with the westerlies to induce increased latent heat uptake and southward Ekman transport of cold water (Alexander and Scott 2008). The surface heat fluxes and advection by Ekman transport hence combine to drive the ENSO-related SST cooling in the North Pacific.

Within the atmospheric bridge paradigm, a relationship between the amplitude of ENSO-related equatorial Pacific SST/precipitation and North Pacific SLP/surface winds is expected. Figure 8 allows assessing such a relationship across the CMIP models. Figure 8a demonstrates that the amplitude of equatorial Pacific ENSO-related precipitation (inferred from a regression of equatorial Pacific precipitation anomalies onto the normalized ENSO index) is indeed linked with the amplitude of ENSO-related equatorial SST anomalies across models (0.78 correlation). In turn, Figure 8b illustrates that the amplitude of ENSO-related precipitation, a proxy for tropical diabatic heating, controls to a large extent the strength of the associated atmospheric planetary wave response channelled toward the North Pacific, and hence the amplitude of the mean SLP in the region of the Aleutian Low across models (-0.79 correlation). Finally, the amplitude of these SLP variations drives the amplitude of the surface wind response in the North Pacific region through geostrophic balance (-0.92 correlation, Fig. 8c, see grey dashed frame on Fig. 6a for the definition of the region over which the zonal wind stress anomaly is estimated). This analysis demonstrates that, across CMIP models, the amplitude of ENSO-related North Pacific SLP and surface wind signals are connected to the amplitude of ENSO through its tropical diabatic heating. This chain that connects the amplitude of ENSO to the ENSO-related surface signature in the North Pacific exists over both interannual and decadal time scales (correlations in parenthesis on each panel of Fig. 8), although the link between the amplitude of ENSO-related equatorial precipitation and the ENSO-related SLP variations in the North Pacific weakens at decadal time scales (-0.57 correlation) compared to interannual time scales (-0.81).

Given the importance of the Aleutian Low fluctuations in characterising the PDO, we now define its ENSO-related and intrinsic parts objectively from an EOF analysis of SLP over the North Pacific region [20°N-60°N; 110°E-110°W]. The contours on Fig. 9a-c show the normalized pattern of the SLP EOF1, i.e. Aleutian Low variability (note that a very similar pattern of Aleutian Low is obtained even if the ENSO signal is removed by a linear regression prior to EOF analysis). This analysis confirms that the leading mode of atmospheric variability over the North Pacific is

associated to a modulation in the intensity of the Aleutian Low. The shaded pattern on Fig. 9a-c shows the ENSO-related SLP signal in the North Pacific (obtained by regression to the ENSO index). The pattern correlation between the Aleutian Low and remotely forced ENSO SLP-signature in the North Pacific is remarkably high in observations (~ 0.9) and also across the CMIP models (0.7 to 0.95). This analysis hence demonstrates that the ENSO remotely-forced SLP signals in the North Pacific project strongly onto the Aleutian Low. In the following, we hence use the principal component of the SLP pattern shown as contours on Fig. 9ac as an index of the Aleutian Low (for which we can isolate the ENSO contribution and independent component by a linear regression). The linear correlation between the ENSO index and the Aleutian Low index for each model and observed dataset (Fig. 9d) will in the following be considered as the *strength of ENSO control* on the North Pacific atmospheric variability. Contrary to the North Pacific SST response to ENSO, which is more delayed in CMIP relative to observations, the delay between the equatorial forcing and mid-latitude atmospheric response is expected to be small due to the fast propagation of atmospheric planetary waves (e.g. Trenberth et al. 1996) and this is verified across models and observations (see lags on Fig. 9d). The weaker ENSO control on the North Pacific atmospheric variability in Class-II models shown in Figure 9d is probably the main reason behind the weaker influence of ENSO on the PDO in those models. This is further demonstrated on Figure 10a that illustrates the strong relationship between the maximum ENSO-PDO lag-correlation and the strength of ENSO control on the Aleutian Low across models (-0.72 correlation, significant at the 99% confidence level). This relationship also exists at interannual and decadal time scales (-0.87 and -0.53 correlation respectively; see Fig. 10bc).

However, the strength of ENSO control on the North Pacific atmospheric variability is likely to depend both on the “signal” (amplitude of the ENSO-driven SLP variability in the North Pacific) and on the “noise” (amplitude of the ENSO-independent pressure variability in the North Pacific):

- (i) As already pointed out from Figure 8, the “signal” depends on the amplitude of ENSO: the larger the ENSO-related equatorial SST signal, the larger the tropical diabatic heating and the stronger the ENSO signature on the North Pacific atmospheric variability is. In the following, the amplitude of ENSO is estimated as the standard deviation of the ENSO time series.
- (ii) The “signal” also depends on the strength of ENSO-driven atmospheric signature over the North Pacific. This amplitude of ENSO-driven North Pacific atmospheric variability is estimated from the linear regression coefficient of Aleutian Low index on the ENSO index (let us remind that with our choice of normalization, the ENSO index contains information about ENSO amplitude in $^{\circ}\text{C}$). We use a simultaneous regression here, since we showed on Fig. 9d that the lag between the equatorial forcing and mid-latitude atmospheric response is

rather small across models and observations. It must however be noted that this simple technique does not allow to extract the possible non-linear interactions existing between ENSO and the Aleutian Low fluctuations.

- (iii) Finally, the amplitude of Aleutian Low fluctuations which is unrelated to ENSO forcing, referred as atmospheric “noise” in the following, could also impact the strength of ENSO control on the North Pacific atmospheric variability: if this atmospheric noise is large, the random-walk part of North Pacific variability will also be large relative to the ENSO-driven one. We estimate the amplitude of this “noise” from the standard deviation of *ENSO-independent* Aleutian Low index (i.e. the ENSO influence is removed from the Aleutian Low index by a linear regression).

Figure 11 shows the scatters of the strength of ENSO influence on the North Pacific atmospheric variability and the three parameters described above. As expected from Figure 8ab, Figure 11a illustrates that the ENSO amplitude contributes to the strength of ENSO influence on the North Pacific atmospheric variability, with a -0.54 correlation between the two parameters. This relationship remains true at interannual (-0.58 correlation) and decadal time scales (-0.51). In addition, Figure 11b shows that the ENSO control is also related to amplitude of the ENSO signature on the North Pacific atmospheric variability (i.e. the amplitude of the Aleutian Low response to a given ENSO amplitude computed by a linear regression between the two), with a -0.58 correlation between these two parameters and similar relationship at interannual and decadal time scales (-0.51 and -0.49 correlation). In contrast, the amplitude of the North Pacific atmospheric noise does not seem to explain the diversity of this control found across the models: Figure 11c indicates that the correlation between these two parameters is not significant at interannual and all time scales. At decadal time scales, a larger ENSO-independent Aleutian Low variability (i.e. “noise”) in the North Pacific indeed leads to a weaker correlation between ENSO and the North Pacific atmospheric variability.

Figure 12 provides another indication of the influence of ENSO amplitude on the PDO amplitude. There is a large range of simulated ENSO and PDO amplitude with some models underestimating the level of variability and others overestimating it. Across this range, there tends to be a linear relationship (~ 0.66) between the ENSO amplitude and PDO amplitude amongst the different datasets (Fig. 12a). Although significant regardless of the time scale considered, this relationship is larger at interannual time scales (Fig. 12b; 0.75 correlation), compared to decadal time scales (Fig. 12c; 0.45 correlation). The strong relationship between the ENSO and PDO amplitudes at interannual time scales is in agreement with the earlier studies that identified ENSO as one of the

major forcing of the PDO at this time scale (e.g. Alexander 1990; Lau and Nath 1994; Lau and Nath 1996; Alexander et al. 2002; Newman et al. 2003; Schneider and Cornuelle 2005).

5. Summary and discussion

5.1. Summary

In this paper, we have assessed the ENSO-PDO relationship in CMIP models and observations. CMIP models overestimate the time lag between ENSO and the PDO, this lag being 1 to 2 months in observations and 4 to 8 months in most of the CMIP models. Not accounting for this delayed PDO response to ENSO leads to an underestimation of ENSO influence on the PDO in CMIP models. When this time lag is taken into account, about half of the 32 CMIP models (Class-I) exhibit a maximum ENSO-PDO lag-correlation larger than 0.5 that lies within the observed range. The other half (Class-II) of the models underestimates this correlation (<0.5). The auto-regressive model of PDO proposed by Newman et al. (2003), which accounts for the north Pacific oceanic memory through re-emergence, ENSO and atmospheric white noise forcing, allows reproducing PDO time series with an average skill of 0.7 correlation in observations and Class-I CMIP models but the skill is poor for Class-II models (an average correlation of 0.45). This auto-regressive model further captures the main PDO spectral characteristics in most of the CMIP models, regardless of the strength of their ENSO-PDO correlation. Only 5 models out of 32 display a decadal (10-30 yrs window) spectral peak that cannot be explained from a combination of ENSO and stochastic noise forcing. This analysis hence suggests that for majority of the models, it is *not* necessary to invoke other mechanisms (e.g. ocean dynamics) to explain the PDO spectrum at decadal and longer time scales.

The PDO pan-Pacific pattern is different between Class-I (i.e. models showing realistic ENSO-PDO relationship) and Class-II (underestimated ENSO-PDO relationship) models. While the PDO pattern is relatively well reproduced in the North Pacific for most models (despite a westward shift in the position of the North Pacific cooling to the Kuroshio extension region), Class-I and Class-II models differ in their ability to reproduce the tropical and south Pacific signature of the PDO. While most of the CMIP models underestimate the PDO-related equatorial warming and south Pacific cooling, this bias is much more accentuated in Class-II models. The strong relationship between the amplitude of the PDO-related equatorial warming and south Pacific cooling in CMIP models indicates that the inter-hemispheric nature of the pan-Pacific PDO is due to ENSO forcing, a coherent forcing to the mid-latitudes of both hemispheres through the atmospheric bridge. We have further examined the reasons behind the diversity of the ENSO-PDO relationship in CMIP models. Results indicate that models with larger ENSO-PDO correlation exhibit a stronger ENSO-control on

the North Pacific sea-level pressure and wind variability. The strength of this control is related to both ENSO amplitude and the amplitude of ENSO imprint on the North Pacific SLP variability in CMIP models. The influence of ENSO amplitude on the PDO is further highlighted by the high correlation between the ENSO and PDO amplitude across the CMIP models.

5.2. Discussion

Half of the CMIP models analysed in the present study display an ENSO-PDO correlation comparable to that observed (~ 0.6). For the other half, the ENSO forcing on the PDO is underestimated because of an underestimation of either ENSO amplitude or strength of ENSO teleconnection to North Pacific sea-level pressure and winds (or both) in the models. The fact that half of the CMIP models accurately capture the strength of the ENSO influence on the PDO appears contradictory with previous studies on this topic (Furtado et al. 2011; Park et al. 2013). For instance, Furtado et al. (2011) concluded that the influence of ENSO on the PDO is very weak or non-existent in most of the CMIP3 models, with only one third of the CMIP3 models having a significant (but weak compared to observation) correlation between ENSO and the PDO. We demonstrate that this discrepancy is at least partly related to methodological aspects. Furtado et al. (2011) and Park et al. (2013) indeed derived their conclusions based on a simultaneous correlation between ENSO and PDO indices. While the relatively small lag of the PDO to ENSO (one to two months) justifies this approach in observations, using a simultaneous ENSO-PDO correlation is more problematic for CMIP models, for which PDO generally lags ENSO by 4 to 8 months. Not accounting for this lag generally results in an underestimated ENSO influence on the PDO in most CMIP models. This is verified on Figure 3, which compares the simultaneous and maximum lag-correlation between ENSO and PDO indices: not accounting for the lag weakly impacts the ENSO-PDO correlation in observations, but results in a systematic underestimation in CMIP models. This overestimated lag of PDO in response to ENSO in CMIP models is a far more systematic bias (only one model does not overestimate it) than the underestimation of the ENSO influence on the PDO. As these biases may have important consequences on the forecast of the North Pacific variability from seasonal to decadal time scales (Guemas et al. 2012), further studies are therefore required to understand the causes of these biases and ultimately to correct them.

This study also shows that the underestimation of the ENSO influence on the PDO in half of the CMIP models can be traced back to both underestimated ENSO amplitude and ENSO teleconnection to the North Pacific SLP and wind variability. From a qualitative visual assessment, Furtado et al. (2011) suggested that CMIP3 models do not accurately capture ENSO influence on the PDO because the pattern of ENSO teleconnection in the North Pacific does not project strongly onto and the

Aleutian Low pattern in these models. In contrast, our study provides quantitative evidences that CMIP models generally capture both the location of the North Pacific ENSO signature and of the Aleutian Low well and that ENSO teleconnection over the North Pacific projects well onto the Aleutian Low for most models (Figure 9). Our analysis further indicates that it is the amplitude rather than the pattern of ENSO signature in mid-latitudes that is faulty in Class-II models. Whether this diversity can be related to mean state biases (such as the westward shift in tropical ENSO SST variability, strength/location of the upper level jet or of the Aleutian Low) deserves further investigations.

The PDO spectrum is consistent with the integration of ENSO and stochastic forcing by the oceanic mixed layer in most of the CMIP models. Spectral peaks at decadal time scales (10-30 years window) that cannot be explained from ENSO and stochastic forcing are seen only in 5 CMIP models out of 32. For these models other mechanisms such as ocean dynamics (gyre circulation, planetary waves) or other air-sea coupled processes need to be invoked to account for a statistically significant spectral peak relative to the red spectrum predicted by the Newman et al. (2003) model. Ocean dynamics and local air-sea coupling may however still play a role in other models at multi-decadal and centennial time scales as suggested by a number of previous studies (Deser and Blackmon 1995; Nakamura et al. 1997; Schneider and Cornuelle 2005; Wu et al. 2003; Park et al. 2013).

One of the strong motivations for this study was to evaluate Pacific decadal SST variability in CMIP models in view of prospects for decadal climate predictions. The main source of PDO predictability is the ENSO forcing. We have shown that the strength of the ENSO influence on the PDO was tightly related to both the amplitude of ENSO and the strength of ENSO signature in mid-latitudes. Those are hence important metrics to be monitored in models to be used for decadal forecasts. Understanding the causes of the biases that can affect the ENSO-teleconnection is also important. The depth of the winter mixed layer in the North Pacific could be a possible cause for the overestimated lag of the PDO response to ENSO in CMIP models (Lienert et al. 2011). Identifying the biases that can lead to a misrepresentation of ENSO signature over the North Pacific (e.g. biases in ENSO-related tropical rainfall patterns, in the location of the Aleutian Low and/or the jet that channels the equatorial signal towards higher latitudes) are also important for the establishment of decadal climate predictions.

Acknowledgements: The lead author is supported by financial assistance and research facilities of CSIR-NIO, India. This research was sponsored under the Agence Nationale pour la Recherche (ANR) MORDICUS project ANR-13-SENV-0002. This work was done while ML was a visiting

scientist at the CSIR-NIO, under Institut de Recherche pour le Développement (IRD) funding. JV and TI also acknowledge IRD support for regular visits to CSIR-NIO. We thank the anonymous reviewer for the valuable comments that helped to improve the manuscript. This is CSIR-NIO contribution No. XXXXX.

References:

- Alexander MA (1990) Simulation of the response of the North Pacific Ocean to the anomalous atmospheric circulation associated with El Niño. *Clim Dyn* 5:53–65. doi: 10.1007/BF00195853
- Alexander MA, Bladé I, Newman M, et al (2002) The Atmospheric Bridge: The Influence of ENSO Teleconnections on Air–Sea Interaction over the Global Oceans. *J Climate* 15:2205–2231.
- Alexander MA, Deser C (1995) A mechanism for the recurrence of wintertime midlatitude SST anomalies. *J. Phys. Oceanogr.*, **25**, 122–137.
- Alexander MA, Scott JD (2008) The Role of Ekman Ocean Heat Transport in the Northern Hemisphere Response to ENSO. *J. Climate*, **21**, 5688–5707.
- Cleveland RB, Cleveland WS, McRae JE and Terpenning I (1990) STL:A Seasonal-Trend Decomposition Procedure Based on Loess. *Journal of Official Statistics* 6:3-73
- Compo GP, Whitaker JS, Sardeshmukh PD, et al (2011) The Twentieth Century Reanalysis Project. *QJRM* 137:1–28. doi: 10.1002/qj.776
- Deser C, Alexander MA, Timlin MS (2003) Understanding the Persistence of Sea Surface Temperature Anomalies in Midlatitudes. *J. Climate*, **16**, 57–72.
- Deser C, Blackmon ML (1995) On the relationship between tropical and North Pacific sea surface temperature variations. *J Climate*. *J. Climate*, **8**,1677–1680.
- Deser C, Phillips AS, Tomas RA, et al (2012) ENSO and Pacific Decadal Variability in the Community Climate System Model Version 4. *J Climate* 25:2622–2651.
- Di Lorenzo E, Schneider N, Cobb KM, Chhak K, Franks PJS, Miller AJ, McWilliams JC, Bograd SJ, Arango H, Curchister E, Powell TM and Rivere P (2008) North Pacific Gyre Oscillation links ocean climate and ecosystem change. *Geophys Res Lett* 35:L08607, doi:10.1029/2007GL032838
- Easterling DR, Wehner MF (2009) Is the climate warming or cooling? *Geophys Res Lett* 36:L08706. doi: 10.1029/2009GL037810
- England MH, McGregor S, Spence P, et al (2014) Recent intensification of wind-driven circulation in the Pacific and the ongoing warming hiatus. *Nature Climate change* 4:222–227.
- Folland CK (2002) Relative influences of the Interdecadal Pacific Oscillation and ENSO on the South Pacific Convergence Zone. *Geophys Res Lett* 29:1643. doi: 10.1029/2001GL014201
- Frankignoul C, Hasselman K (1977) Stochastic climate models. part 2: Application to sea-surface temperature variability and thermocline variability. *Tellus* 29:284–305

- Furtado JC, Di Lorenzo E, Schneider N (2011) North Pacific Decadal Variability and Climate Change in the IPCC AR4 Models. *J Climate* 24:3049–3067. doi: 10.1175/2010JCLI3584.1
- Garreaud R, Battisti DS (1999) Interannual (ENSO) and Interdecadal (ENSO-like) Variability in the Southern Hemisphere Tropospheric Circulation*. *J Climate* 12:2113–2123.
- Guemas V, Doblas Reyes FJ, Lienert F, et al (2012) Identifying the causes of the poor decadal climate prediction skill over the North Pacific. *J Geophys Res.* 1984-2012, **117** doi: 10.1029/2012JD018004
- Kaplan A, Cane MA, Kushnir Y, Clement AC (1998) Analyses of global sea surface temperature 1856-1991. *J. Geophys. Res.*, **103**, 18 567–18 589, doi:10.1029/97JC01736
- Klein SA, Soden BJ, Lao NC (1999) Remote sea surface temperature variations during ENSO: Evidence for a tropical atmospheric bridge. *J. Climate*, **12**, 917–932, doi:10.1175/1520-0442(1999)0122.0.CO;2
- Knapp KR, Kruk MC, Levinson DH, et al (2010) The International Best Track Archive for Climate Stewardship (IBTrACS). <http://dxdoiorg/101175/2009BAMS27551> 91:363–376.
- Kosaka Y, Xie SP (2013) Recent global-warming hiatus tied to equatorial Pacific surface cooling. *Nature* **501**, 403–407
- Kwon M, Yeh S-W, Park Y-G, Lee Y-K (2012) Changes in the linear relationship of ENSO-PDO under the global warming. *Int J Climatol* 33:1121–1128. doi: 10.1002/joc.3497
- Lau N-C, Nath MJ (1996) The Role of the “Atmospheric Bridge” in Linking Tropical Pacific ENSO Events to Extratropical SST Anomalies. *J. Climate*, **9**, 2036–2057.
- Lau NC, Nath MJ (1994) A modeling study of the relative roles of tropical and extratropical SST anomalies in the variability of the global atmosphere-ocean system. *J. Climate*, **7**, 1184-1207
- Lau NC, Nath MJ (2000) Impact of ENSO on the variability of the Asian-Australian monsoons as simulated in GCM experiments. *J Climate* 13:4287–4309.
- Lienert F, Fyfe JC, Merryfield WJ (2011) Do Climate Models Capture the Tropical Influences on North Pacific Sea Surface Temperature Variability? *J Climate* 24:6203–6209. doi: 10.1175/JCLI-D-11-00205.1
- Liu Z (2012) Dynamics of Interdecadal Climate Variability: A Historical Perspective*. *J Climate* 25:1963–1995. doi: 10.1175/2011JCLI3980.1
- Mantua NJ, Hare SR, Zhang Y, et al (1997) A Pacific Interdecadal Climate Oscillation with Impacts on Salmon Production. *Bull. Amer. Meteor. Soc.*, **78**, 1069–1079
- McPhaden MJ, Zebiak SE, Glantz MH (2006) ENSO as an Integrating Concept in Earth Science. *Science* 314:1740–1745. doi: 10.1126/science.1132588
- Meehl GA, Arblaster JM, Fasullo JT, et al (2011) Model-based evidence of deep-ocean heat uptake during surface-temperature hiatus periods. *Nature Climate change* 1:360–364. doi: 10.1038/nclimate1229

- Meehl GA, Covey C, Taylor KE (2007) The WCRP CMIP3 multimodel dataset: A new era in climate change research. *Bull. Amer. Meteor. Soc.*, **88**, 1383–1394.
- Meehl GA, Goddard L, Boer G, et al (2014) Decadal Climate Prediction: An Update from the Trenches. *Bull. Amer. Meteor. Soc.*, 95:243–267. doi: 10.1175/BAMS-D-12-00241.1
- Namias J, Born RM (1974) Further studies of temporal coherence in North Pacific Sea surface temperatures. *Journal of Geophysical Research: Oceans* (1978–2012) 79:797–798.
- Newman M (2013) An Empirical Benchmark for Decadal Forecasts of Global Surface Temperature Anomalies. *J Climate* 26:5260–5269. doi: 10.1175/JCLI-D-12-00590.1
- Newman M (2007) Interannual to Decadal Predictability of Tropical and North Pacific Sea Surface Temperatures. *J Climate* 20:2333–2356. doi: 10.1175/JCLI4165.1
- Newman M, Compo GP, Alexander MA (2003) ENSO-forced variability of the Pacific decadal oscillation. *J Climate*, vol. 16, No. 23
- Oshima K, Tanimoto Y (2009) An Evaluation of Reproducibility of the Pacific Decadal Oscillation in the CMIP3 Simulations. *JMSJ* 87:755–770. doi: 10.2151/jmsj.87.755
- Park J-H, An SI, Yeh S-W, Schneider N (2013) Quantitative assessment of the climate components driving the pacific decadal oscillation in climate models. *Theor Appl Climatol* 112:431–445. doi: 10.1007/s00704-012-0730-y
- Pierce DW, Barnett TP, Latif M (2000) Connections between the Pacific Ocean Tropics and Midlatitudes on Decadal Timescales. *J Climate* 13:1173–1194.
- Power S, Tseitkin F, Mehta V, Lavery B (1999) Decadal climate variability in Australia during the twentieth century. *Int Jour of Climatology* vol. 19, 2, 169-184
- Qiu B, Schneider N, Chen S (2007) Coupled Decadal Variability in the North Pacific: An Observationally Constrained Idealized Model*. *J Climate* 20:3602–3620.
- Rayner NA, Parker DE, Horton EB, et al (2003) Global analyses of sea surface temperature, sea ice, and night marine air temperature since the late nineteenth century. *Journal of Geophysical Research: Oceans* (1978–2012) 108:4407. doi: 10.1029/2002JD002670
- Schneider N, Cornuelle BD (2005) The Forcing of the Pacific Decadal Oscillation* *J. Climate*, **18**, 4355–4357.
- Shakun JD, Shaman J (2009) Tropical origins of North and South Pacific decadal variability. *Geophys Res Lett* 36:L19711. doi: 10.1029/2009GL040313
- Smith TM, Reynolds RW, Peterson TC, Lawrimore J (2008) Improvements to NOAA’s Historical Merged Land–Ocean Surface Temperature Analysis (1880–2006). *J Climate* 21:2283–2296. doi: 10.1175/2007JCLI2100.1
- Storch HV, Zwiers FW (1999) *Statistical Analysis in Climate Research*. Cambridge University Press, Cambridge
- Taylor KE, Stouffer RJ, Meehl GA (2012) An Overview of CMIP5 and the Experiment Design. *Bull.*

Amer. Meteor. Soc. 93:485–498. doi: 10.1175/BAMS-D-11-00094.1

Trenberth KE, Branstator GW, Karoly D, et al (1998) Progress during TOGA in understanding and modeling global teleconnections associated with tropical sea surface temperatures. *Journal of Geophysical Research: Oceans* (1978–2012) 103:14291–14324. doi: 10.1029/97JC01444

Woodruff SD, Worley SJ, Lubker SJ, et al (2011) ICOADS Release 2.5: extensions and enhancements to the surface marine meteorological archive. *Int J Climatol* 31:951–967. doi: 10.1002/joc.2103

Wu L, Liu Z, Gallimore R, et al (2003) Pacific decadal variability: The tropical Pacific mode and the North Pacific mode. *J Climate*, Vol. 16, No.8

Yim BY, Kwon M, Min HS, Kug J-S (2014) Pacific Decadal Oscillation and its relation to the extratropical atmospheric variation in CMIP5. *Clim Dyn* 44:1521–1540. doi: 10.1007/s00382-014-2349-4

Yin X, Gleason BE, Compo GP, Matsui N (2008) The International Surface Pressure Databank (ISPD) land component version 2.2., National Climatic Data Center, Asheville, NC, pp.1-12, 2008.

Zhang Y, Wallace JM, Battisti DS (1997) ENSO-like interdecadal variability: 1900-93. *J Climate* **10**, 1004-1020.

CMIP3 models				
No.	Model Name	Short Name	Length (yr)	Class
1	CGCM3.1	CGCM	500	II
2	GFDL-CM2.0	GFDL2.0	500	II
3	GFDL-CM2.1	GFDL2.1	500	I
4	GISS-AOM	GISSAO	250	II
5	GISS-ER	GISSER	500	II
6	IPSL-CM4	IPSL4	500	I
7	MIROC3.2(m)	MIROC3	500	I
8	ECHO-G	ECHOG	340	I
9	MRI-CGCM2.3.2	MRI2.3.2	350	II
10	UKMO-HadCM3	HadCM3	340	II
CMIP5 models				
11	BCC-CSM1.1	BCCCSM	500	II
12	CanESM2	CanESM	500	I
13	CCSM4	CCSM4	500	I
14	CNRM-CM5	CNRM	500	II
15	CSIRO-Mk3.6.0	CSIRO	500	I
16	FIO-ESM	FIO	500	II
17	GFDL-CM3	GFDL3	500	I
18	GFDL-ESM2G	GFDL2G	500	II
19	GFDL-ESM2M	GFDL2M	500	I
20	GISS-E2-R	GISSE2R	500	II
21	HadGEM2-ES	HadGEM	500	I
22	INM-CM4	INMCM	500	II
23	IPSL-CM5A-LR	IPSL-LR	500	I
24	IPSL-CM5A-MR	IPSL-MR	300	I
25	IPSL-CM5B-LR	IPSL5B	300	II
26	MIROC5	MIROC5	500	I
27	MPI-ESM-LR	MPI-LR	500	I
28	MPI-ESM-MR	MPI-MR	500	II
29	MPI-ESM-P	MPI-P	500	I
30	MRI-CGCM3	MRI3	500	II
31	NorESM1-ME	Nor-ME	252	I
32	NorESM1-M	Nor-M	500	I

Table 1: List of models analysed in the present study from CMIP3 and CMIP5 database. Model name, short name used in figures and discussion, length of the simulation and Class of the model (see text) are also given.

Model	Period	Class
CCSM4	10 – 20	I
MRI-CGCM2.3.2	10 – 15	II
MRI-CGCM3	10 – 20	II
BCC-CSM1.1	10 – 20	II
GISS-ER	10 – 30	II

Table 2: Models that display a peak at decadal time scales which is not explained by the AR1 model (eqn. 1). The time-scale range of this peak is indicated in the second column.

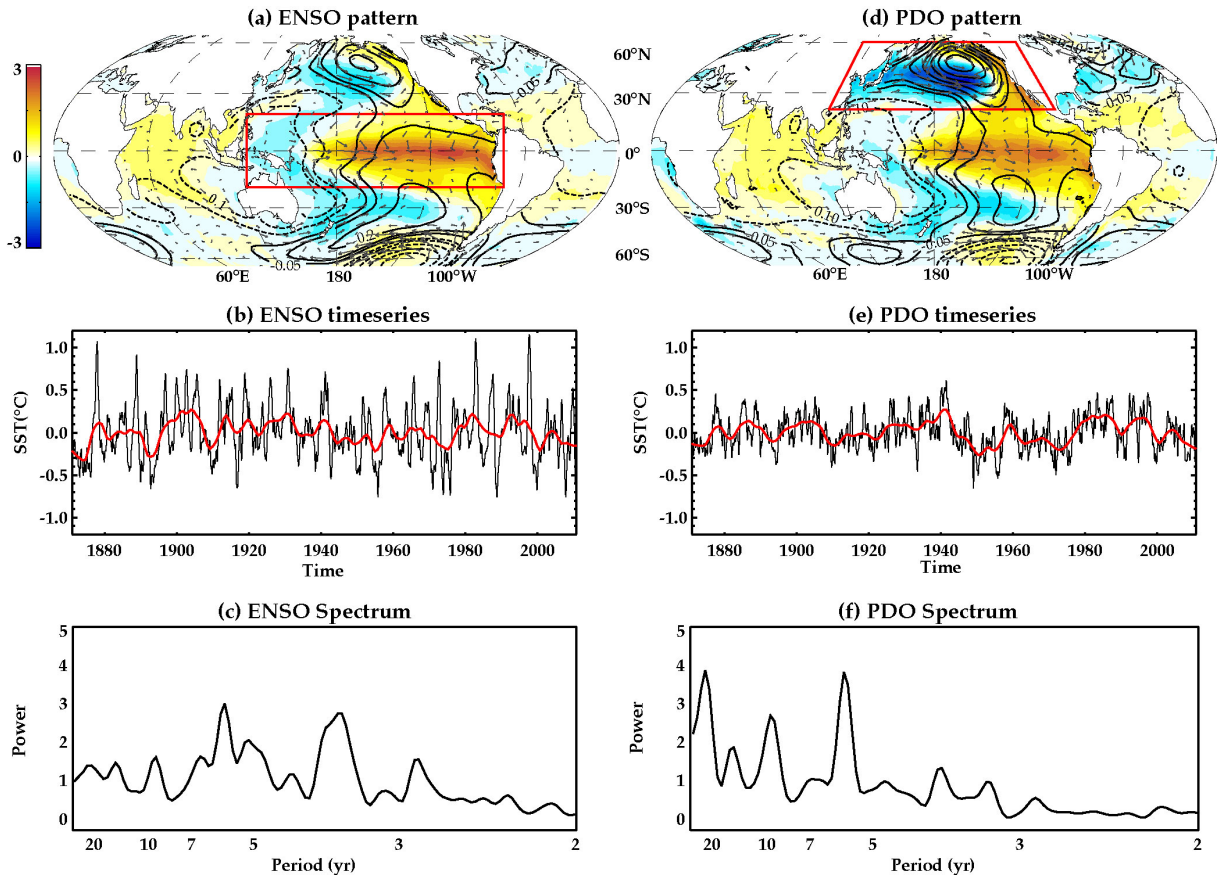


Figure 1: El Niño Southern Oscillation defined as **(a)** the leading empirical orthogonal function (EOF) of monthly SST anomalies over the tropical Pacific (120°E-80°W; 20°N-20°S, red frame) for HadISST dataset over the 1871-2010 period, its **(b)** associated principal component (PC) time series (black curve) and corresponding decadal (> 7yrs) component (red curve) and **(c)** its (normalized PC) power spectrum. The EOF pattern is normalized by its spatial root mean square (RMS) so that the PC is a measure of the ENSO amplitude. The spatial pattern is obtained globally by regressing the SST anomalies (color), wind-stress anomalies (vectors) and mean sea-level pressure anomalies (contours) on to the PC. **(d-f)** Same as **(a-c)** but for **Pacific Decadal Oscillation** defined as the leading EOF of monthly SST anomalies over the North Pacific (110°E-110°W; 20°N-60°N, red frame on (d)). Monthly SST anomalies are calculated by removing the mean seasonal cycle and a five-month running mean is applied on this SST anomalies. Global mean SST time series and a linear trend are further removed from each grid point before computing the EOFs. SST spatial pattern and spectra are unit less while SST time series are in °C and wind vectors have $\text{N.m}^{-2}.\text{°C}^{-1}$ units. See section 2.4 for details of the power spectrum calculation.

ENSO PDO Lag-correlation

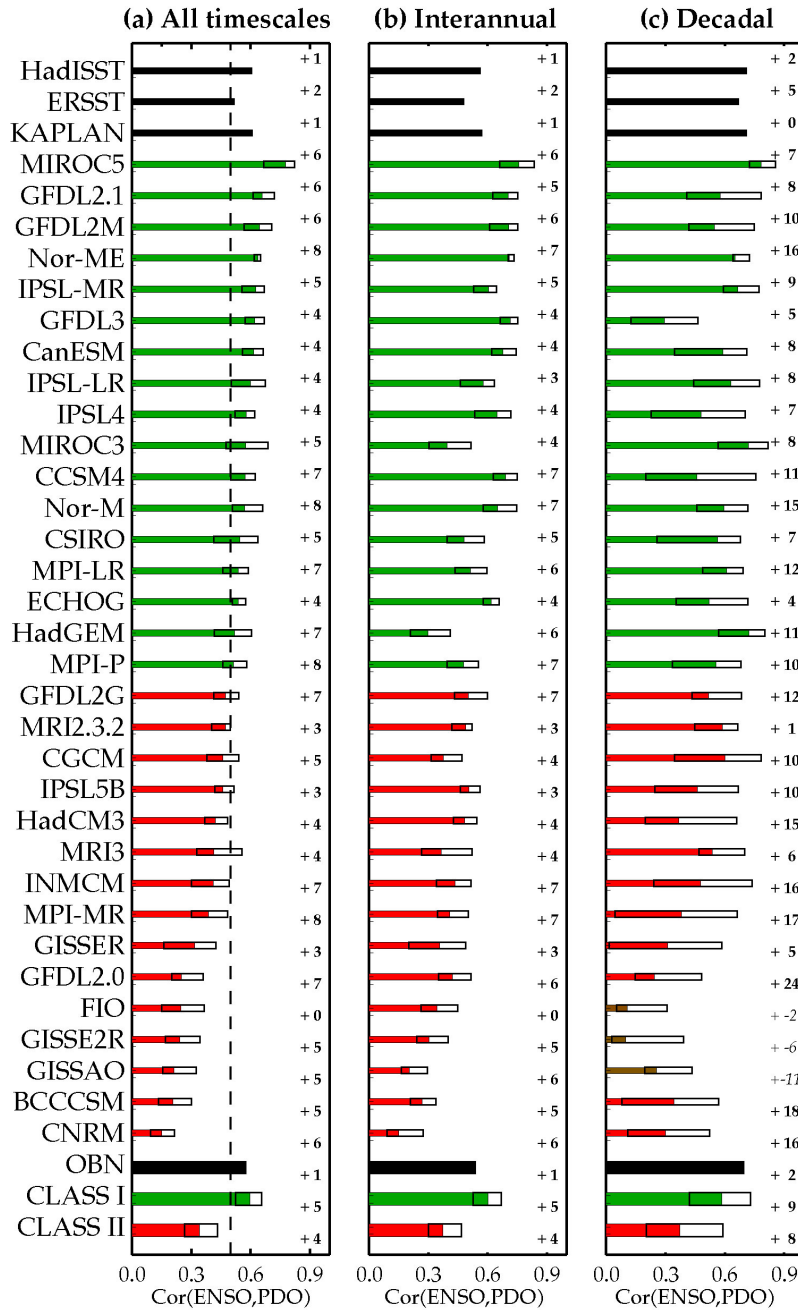


Figure 2: Maximum lag-correlation coefficient between the ENSO and PDO time series at (a) all time scales (including both interannual and decadal periodicities), (b) interannual and (c) decadal time scales. The number shown to the right of each bar indicates the lag (in month) of the maximum correlation, with positive lag indicates ENSO leading the PDO. The lag is indicated in italic when the correlation is not significantly different from zero based on a t-test. CMIP models are divided into two classes depending on this maximum lag-correlation between PDO and ENSO at all time scales: Class-I models (green bars) with correlation above 0.5 and Class-II models (red bars) below that threshold. The transparent bar at the tip of the colour bars indicates the minimum and maximum correlation obtained for each CMIP model when evaluating the correlation over sliding windows of the same length of the observed datasets (i.e. 140 years). Average correlation for observations, Class-I and Class-II models are indicated as thick bars on the bottom of each panel along with the average lag and uncertainty levels.

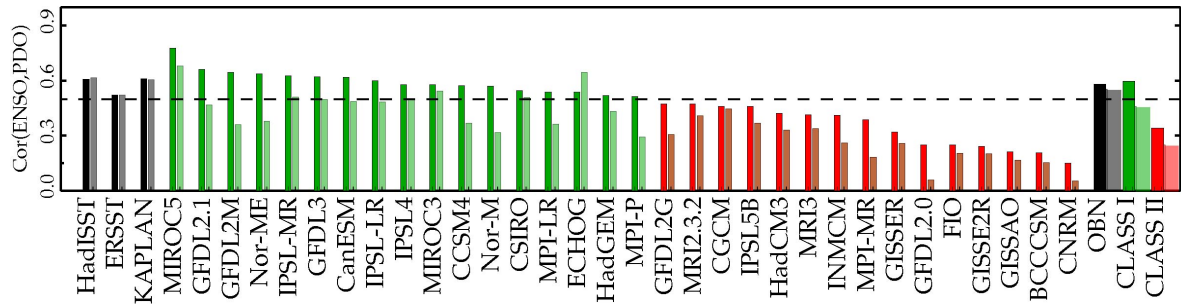


Figure 3: Maximum lag-correlation (dark shading) and simultaneous correlation (light shading) between the DJF ENSO and PDO indices for all models and observations.

Newman's model

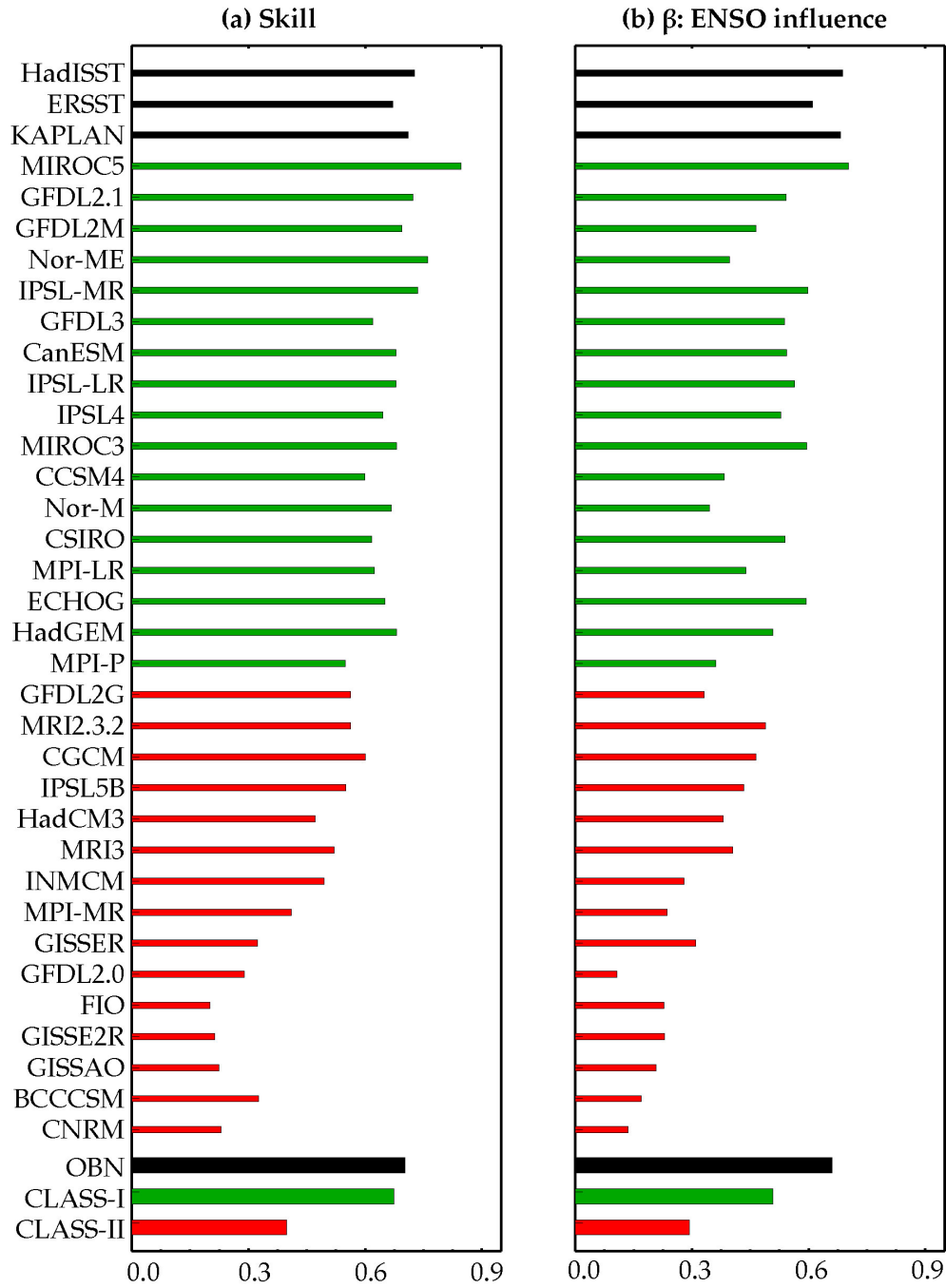


Figure 4: (a) Correlation between original PDO time series and computed PDO time series using the AR-1 model (equation 1) for CMIP models and observations and (b) ENSO coefficient obtained for the AR-1 model. Class-I models are indicated in green and Class-II models in red as defined in the text and in the caption of Figure 2. Average value of these metrics for observations, Class-I and Class-II models are shown as thick bars on the bottom of each panel.

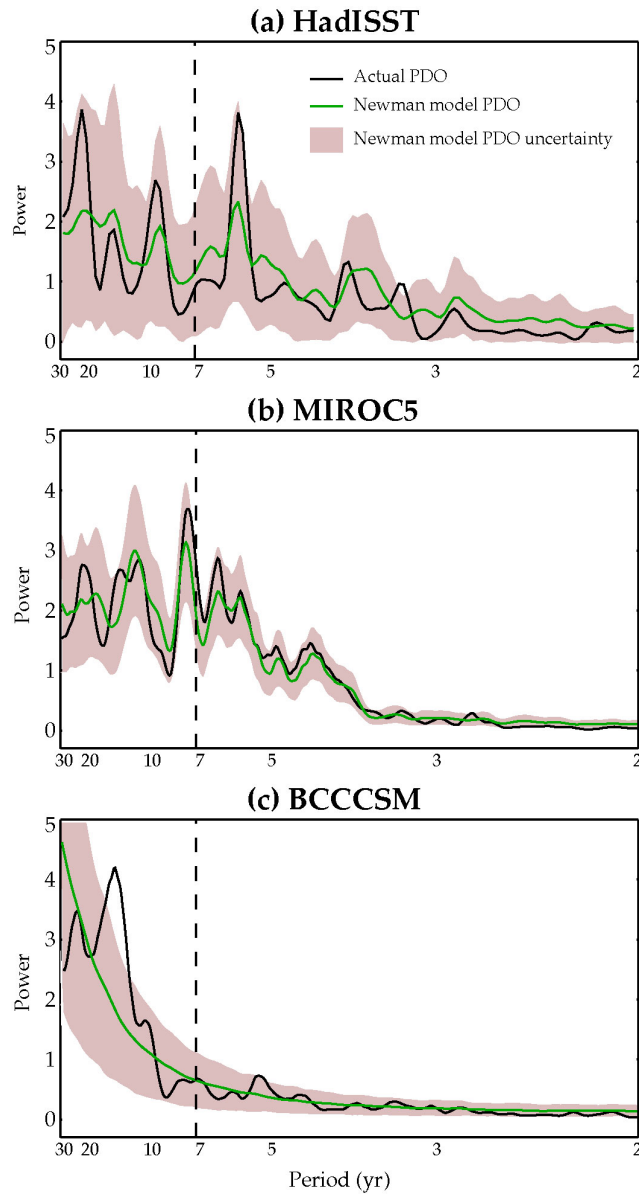


Figure 5: Power spectrum of the normalized PDO time series (black), ensemble mean spectrum of thousand “model” spectra computed from thousand model time series (by equation 1; green) for **(a)** HadISST, **(b)** MIROC5 and **(c)** BCC-CSM2-1. The 95% confidence interval for the model spectrum (shown by shading) is determined by a two-sided t-distribution of 1000 samples of "model" spectra.

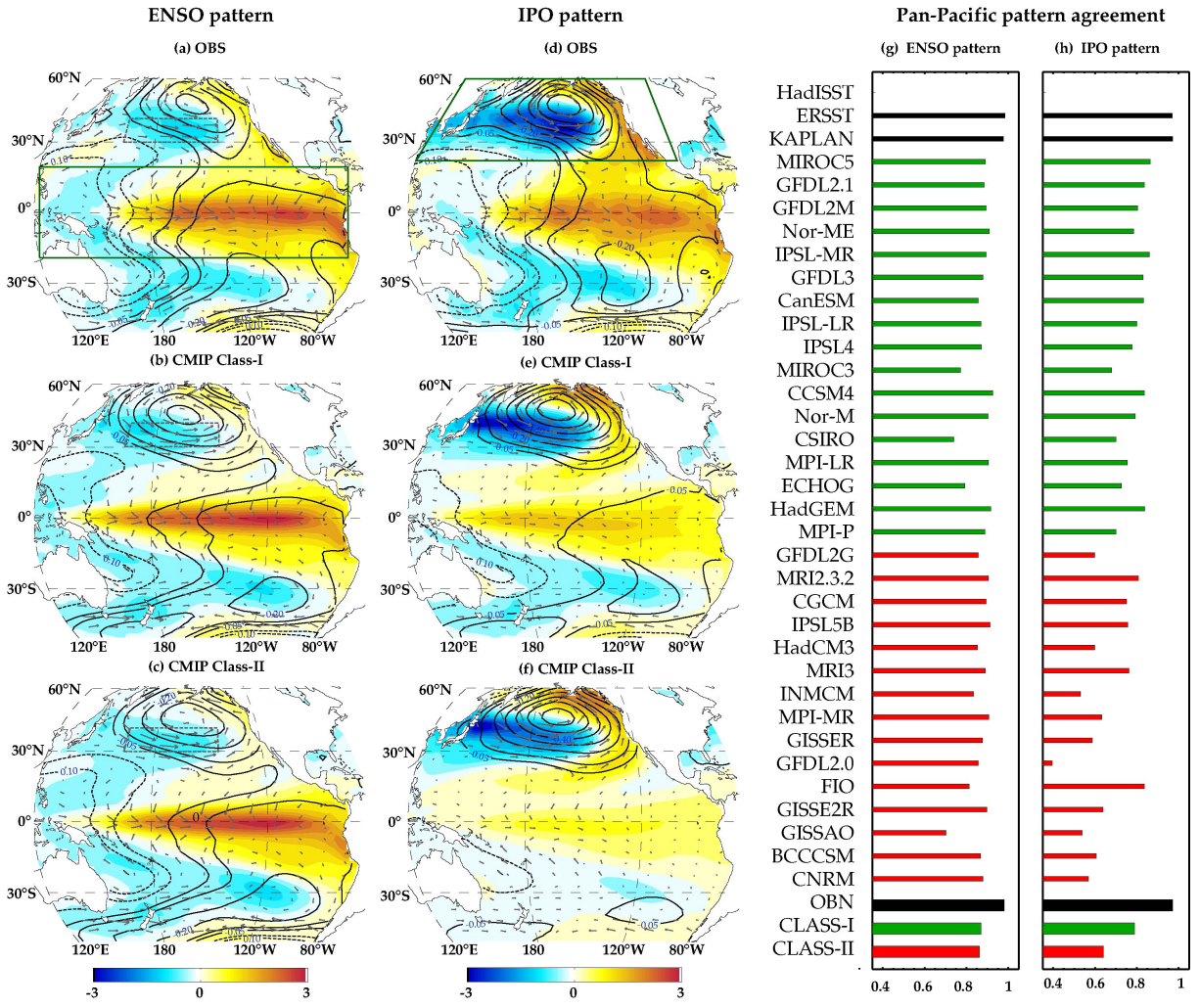


Figure 6: Pan-Pacific SST, wind stress and sea-level pressure signature of ENSO for **(a)** HadISST and 20thC (as in Fig. 1a), **(b)** Class-I and **(c)** Class-II CMIP models ensemble mean (Class-I and Class-II models are defined in the text and in the caption of Figure 2). ENSO pattern is defined as the leading EOF of SST anomalies in the tropical Pacific (120°E-80°W; 20°N-20°S, green rectangle on panel a) normalized by its spatial root mean square so that the PC is a measure of the ENSO amplitude. The pan-Pacific signature of ENSO is obtained by regressing the SST (color), sea-surface pressure (contours) and wind stress (vectors) anomalies onto the first PC time series. **(d-f)** Same as (a-c) but for the pan-Pacific signature of the PDO which is defined as the leading EOF of SST anomalies over the North Pacific (110°E-110°W; 20°N-60°N, green rectangle on panel d). SST pan-Pacific pattern correlation of each dataset with HadISST pattern for **(g)** ENSO and **(h)** PDO. SST patterns are unit less and wind stress vectors have N.m⁻².°C⁻¹ units. On panels g and h, observational datasets are plotted in black, Class-I models in green and Class-II models in red. Average values for observations, Class-I and Class-II models are indicated as thick bars on the bottom of each panel. The gray dashed rectangle on panels (a-c) indicates the region where the mean zonal wind stress is averaged for Figure 8c.

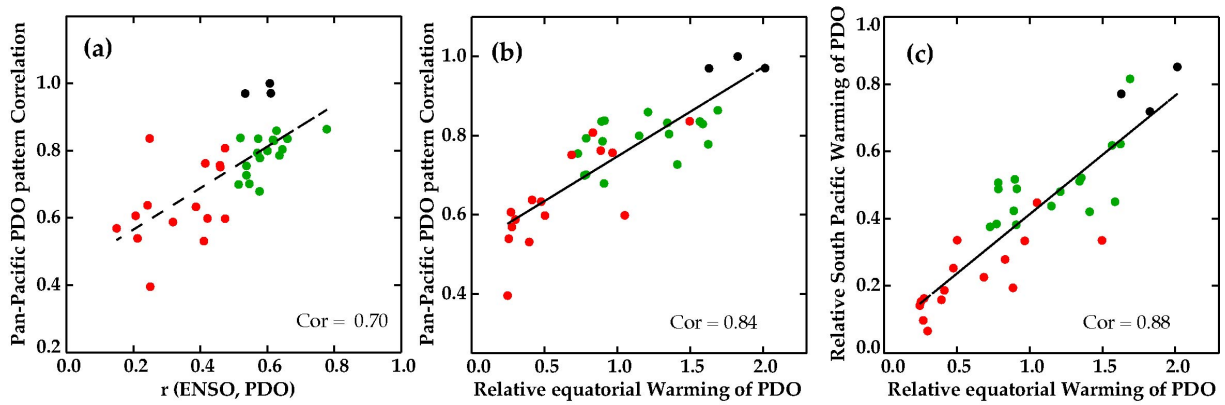


Figure 7: (a) Scatter of the Pan-Pacific PDO pattern correlation of each dataset with HadISST pattern shown in Figure 6h against the maximum lag-correlation between the ENSO and the PDO time series shown in Figure 2a for all CMIP (red for Class-II and green for Class-I models) and observational (black) datasets. (b) Same as (a) but between Pan-Pacific PDO pattern correlation and the relative amplitude of the PDO SST signature in the tropical Pacific. (c) Same but for the relative amplitude of PDO SST in South Pacific against relative amplitude of PDO SST in the tropical Pacific. The relative amplitude of the PDO SST signature in the tropical and South Pacific are computed by the spatial root mean square of re-projected SST pattern of the PDO in the tropical Pacific ($120^{\circ}\text{E}-80^{\circ}\text{W}$; $20^{\circ}\text{N}-20^{\circ}\text{S}$) and South Pacific ($120^{\circ}\text{E}-80^{\circ}\text{W}$; $20^{\circ}\text{S}-50^{\circ}\text{S}$).

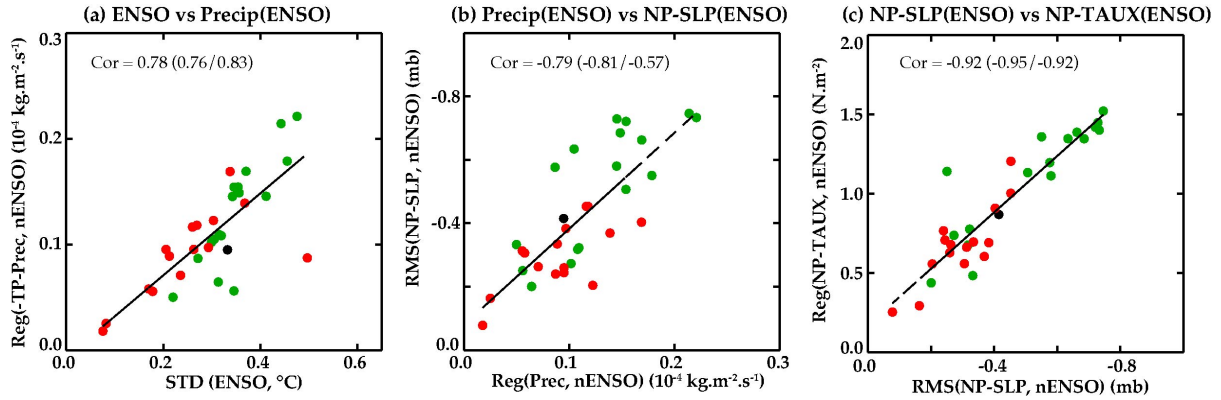


Figure 8: Scatter of (a) the amplitude of ENSO against the ENSO-related precipitation amplitude in the equatorial Pacific [5°N - 5°S ; 130°E - 140°W], (b) ENSO-related precipitation amplitude in the equatorial Pacific against ENSO-related mean sea-level pressure amplitude in the North Pacific [20°N - 60°N ; 110°E - 110°W] (see green frame on Fig. 6d) and (c) ENSO-related mean sea-level pressure in the North Pacific against ENSO-related zonal wind stress in the North Pacific [30°N - 40°N ; 160°E - 150°W] (see dashed frame on Fig. 6a-c) for CMIP models and HadISST/20thC datasets at all time scales. Standard deviation of ENSO time series is considered as the "ENSO amplitude". ENSO-related equatorial precipitation and ENSO-related winds in North Pacific are derived by simple regression of the variable onto the normalized ENSO index. ENSO-related North Pacific SLP variability is defined here from the root-mean square of the point-wise (spatial map) regression coefficient of SLP to the ENSO index within the region [20°N - 60°N ; 110°E - 110°W], and will be more objectively defined from Fig. 9. Correlation coefficient corresponding to each scatter is also given on the upper left of each panel along with the similar correlations individually for interannual and decadal time scales in parenthesis.

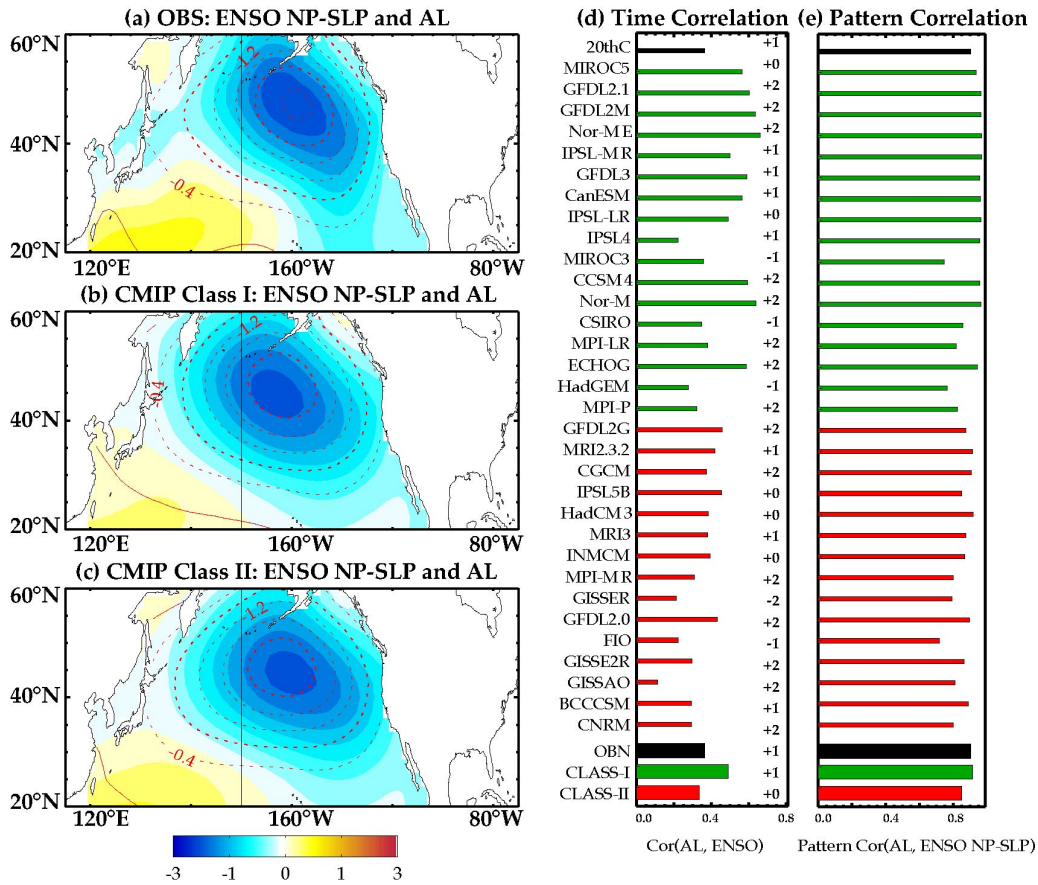


Figure 9: Regression pattern of SLP anomalies in the North Pacific to the ENSO index (color) and pattern of Aleutian Low (derived from the first EOF of North Pacific SLP; contours) at all time scales for **(a)** 20thC reanalysis, **(b)** Class-I and **(c)** Class-II ensemble model mean. Both contours and shaded pattern are normalised by their respective spatial RMS and hence are unit less. **(d)** Maximum lag correlation of the Aleutian Low Index (PC of the first EOF of North Pacific SLP) to the ENSO index at all time scales (the lag of the maximum correlation, in months, is also shown with a positive lag indicates ENSO leads AL). **(e)** Pattern correlation between the Aleutian Low and the ENSO-related SLP anomalies in the North Pacific.

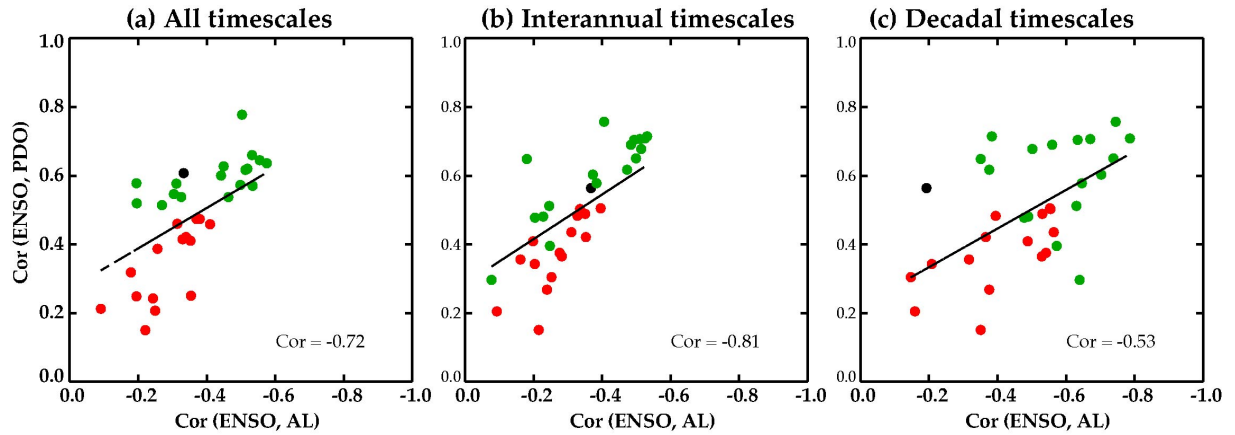


Figure 10: Scatter of the ENSO/PDO maximum lag-correlation (as displayed on Figure 2) against the correlation of ENSO index with Aleutian low index for **(a)** all time scales, **(b)** interannual time scales and **(c)** decadal time scales for CMIP models and HadISST/20thC datasets.

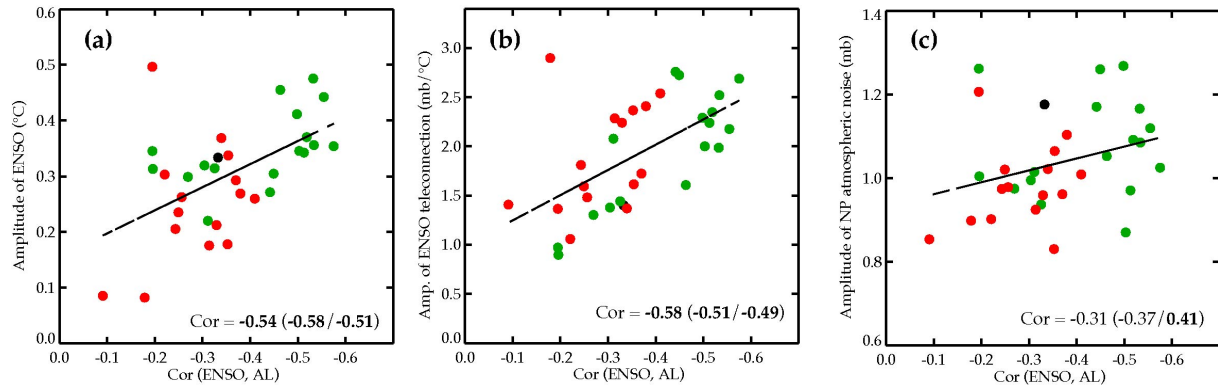


Figure 11: Scatter of the strength of "ENSO-control" on the North Pacific atmospheric variability against (a) the ENSO amplitude, (b) the strength of ENSO teleconnection to North Pacific variability, and (c) atmospheric noise in the North Pacific for CMIP models and HadISST/20thC datasets at all time scales. Correlation coefficients corresponding to each scatter is given on the bottom right of each panel along with the same correlation individually for interannual and decadal time scales in parenthesis. Correlation coefficients that are significant at 95% confidence level are shown in bold letters. See text for the definition of each of the metrics plotted.

ENSO vs PDO Amplitude

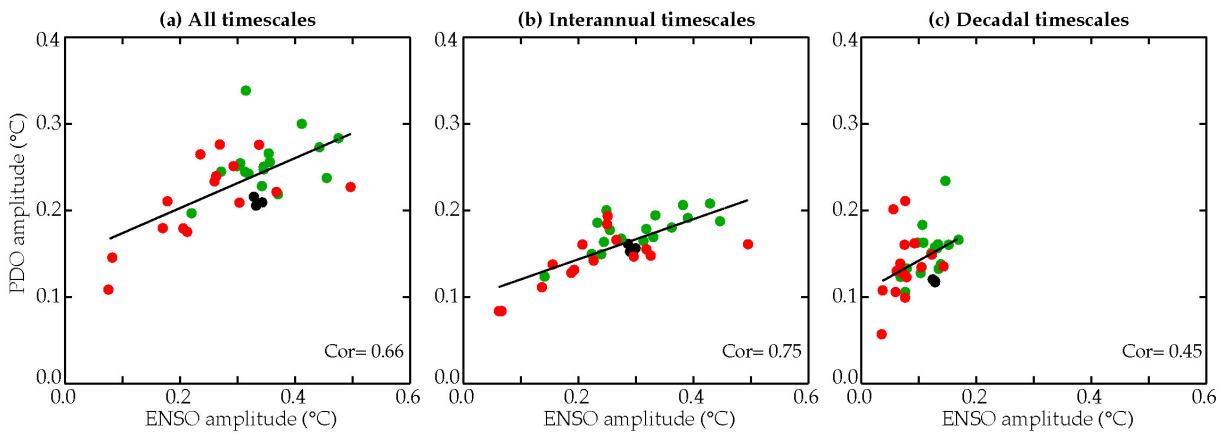


Figure 12: Scatterplot of the ENSO amplitude versus PDO amplitude in CMIP models and the three observational datasets for **(a)** all time scales **(b)** interannual time scales and **(c)** decadal time scales. Amplitude of ENSO and PDO is estimated as the standard deviation of ENSO and PDO indices. Correlation coefficient corresponding to each scatter is given in each panel.